Desalination 631 (2026) 120226

Contents lists available at ScienceDirect

Desalination

journal homepage: www.elsevier.com/locate/desal

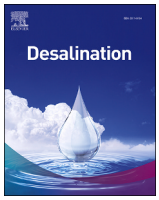

Coupled energy storage and desalination in a hydrogen-mediated acid-base flow battery

Pavel A. Loktionov [a,b,*], Afke G.M. Damen [a], Vojtěch Konderla [a,b], David A. Vermaas [a,b,*]

[a] Department of Chemical Engineering, Delft University of Technology, Van der Maasweg 9, 2629HZ, Delft, the Netherlands
[b] e-Refinery Institute, Leeghwaterstraat 39, 2628CB, Delft, the Netherlands

HIGHLIGHTS

- Hydrogen-mediated acid-base flow battery enables energy storage and seawater desalination.
- The battery achieves 90–97% ion removal and 50% recovery at 31% desalination of 0.5 M NaCl.
- Optimized battery design can lower SEC to 14–18 kJ mol^{-1} at 1–5 mA cm^{-2} current density.
- Compatible with renewables and suitable for decentralized coastal water systems

ARTICLE INFO

Keywords:
Desalination
Energy storage
Flow battery
Neutralization
Water-energy nexus

ABSTRACT

We present a novel concept for coupling energy storage and water desalination using an acid–base flow battery architecture. In this device, electrical energy is stored through the reversible generation of acid and base, while salt is simultaneously removed from a central salt chamber. The device operates with non-toxic, earth-abundant electrolytes - NaOH and HCl - and utilizes hydrogen as an efficient redox mediator, avoiding crossover of redox active species and enabling high reversibility. We demonstrate that the degree of desalination directly impacts the desalination flow battery's open-circuit voltage and internal resistance, with high efficiency achieved at partial desalination. At 7 mA cm^{-2}, the device desalinates 0.5 M NaCl by 31% with 90–97% ion removal efficiency and 50% water recovery. Modelling of specific energy consumption indicates values as low as 14–18 kJ $mol(NaCl)^{-1}$ are achievable using state-of-the-art membranes and compartment designs. This places the device performance in line with leading desalination flow batteries while unlocking additional value through energy storage using abundant chemicals. We propose its use in decentralized coastal grids powered by intermittent renewables, where it can balance energy supply for downstream processes while at the same time desalinating seawater. This work outlines a scalable sustainable approach to address the water-energy nexus using benign and abundant chemicals.

1. Introduction

Freshwater scarcity is increasingly recognized as a critical global challenge with direct implications for human health, food security, and economic development. As of the end of 2025, approximately 17% of the global population lives in regions classified as high water risk, where water scarcity, declining water quality, climatic variability, and governance limitations jointly threaten reliable access to freshwater [1]. This share may exceed 50% by 2050, placing even greater pressure on water resources [1]. At the same time, water scarcity is tightly coupled to energy availability, forming the water–energy nexus [2]: desalination can expand freshwater supplies but is constrained by high energy demand - especially in regions with limited or unstable energy infrastructure [3]. These intertwined limitations call for technologies that address water purification and energy storage in an integrated way [2].

Conventional large-scale desalination technologies – such as seawater reverse osmosis (SWRO) [4], brackish reverse osmosis (BRO) [5], electrodialysis (ED) [5,6], capacitive deionization (CDI) [7], multi-effect distillation (MED) [8], and multi-stage flash distillation (MSF) [9] - deliver high efficiency and reliability, supporting many urban water systems. This limitation has motivated interest in modular systems that combine desalination with decentralized energy storage, enabling

* Corresponding authors at: Department of Chemical Engineering, Delft University of Technology, Van der Maasweg 9, 2629HZ, Delft, the Netherlands.
E-mail addresses: p.a.l.loktionov@tudelft.nl (P.A. Loktionov), d.a.vermaas@tudelft.nl (D.A. Vermaas).

https://doi.org/10.1016/j.desal.2026.120226
Received 19 February 2026; Received in revised form 6 April 2026; Accepted 23 April 2026
Available online 24 April 2026

flexible operation under variable power availability.

In this context, desalination batteries have emerged as a promising class of electrochemical systems that integrate energy storage with salt removal [10,11]. Typically derived from flow battery architectures, these devices employ anion-exchange membranes (AEMs) and cation-exchange membranes (CEMs) to form a central saline-water compartment, where electrochemical redox reactions drive either desalination or salination depending on the operating mode [10].

Yet despite their promise, most reported desalination flow batteries face a fundamental trade-off that limits true system autonomy. They must choose between using scarce, toxic, or expensive redox-active species, or relying on external supplies of chemicals such as acid, base, or oxidants, which undermines system reversibility and autonomy. For example, many systems based on inorganic [12–17] and organic chemistries [18,19] rely on non-benign or costly materials, while desalination fuel cells [20–22] and neutralization flow cells [23–25] achieve desalination by consuming externally produced chemicals, preventing closed-loop operation.

This creates a central trade-off in the field: desalination flow batteries must compromise either on environmental sustainability or operational independence.

In this work, we resolve this trade-off by introducing a hydrogen-mediated acid–base desalination flow battery that enables closed-loop energy storage and salt removal using only earth-abundant, non-toxic chemicals. The device operates using hydrogen as a redox mediator and NaCl-derived acid and base as electrolytes, eliminating the need for external chemical input while preserving high reversibility and desalination functionality (Fig. 1). The proposed device consists of three compartments: an acidic compartment and a basic compartment, each equipped with a hydrogen electrode, and a central saline-water compartment separated by an AEM and a CEM. The hydrogen electrodes enable reversible production and neutralization of acid and base, using hydrogen as an efficient and non-consumable redox mediator (see reactions (1)–(3)). During charging, hydrogen is oxidized at the acidic electrode and regenerated at the alkaline electrode; this process is reversed during discharge. Concurrently, ion transport across the membranes enables controlled desalination or salination of the central stream.

The key electrochemical steps during charging are:

Hydrogen oxidation at the positive electrode in acidic media:

$$H_2 = 2H^+ + 2e^- \quad (1)$$

Hydrogen evolution at the negative electrode in alkaline media:

$$2H_2O + 2e^- = 2OH^- + H_2 \quad (2)$$

Overall net reaction:

$$H_2O = H^+ + OH^- \quad (3)$$

Compared to earlier desalination flow batteries, our architecture eliminates the need for toxic, scarce, or expensive redox-active species. Unlike desalination fuel cells, which suffer from high activation losses associated with oxygen reactions (~0.2 V) [26], our use of hydrogen enables higher reversibility and round-trip efficiency. In contrast to prior hydrogen-looping acid-base systems [25], our membrane arrangement enables desalination directly from saline feedwater – without the need to externally supply acid or base. This allows the system to achieve both desalination and energy storage in a single, self-contained unit.

As such, the device offers a compact and chemical self-sufficient alternative to more complex configurations combining desalination units, electrolysers, and fuel cells – particularly attractive for off-grid, coastal regions lacking hydrogen infrastructure.

In this work, we demonstrate the operating principles of this device and analyze its performance under two coupled operational regimes: charging with simultaneous desalination, followed by discharging with salination. We investigate how energy consumption and efficiency depend on the degree of desalination and show that the system operates most efficiently when treating water at seawater salinity levels (~30 g L^{-1}). We further demonstrate how cell design and operating conditions can be adjusted to maintain high efficiency at deeper desalination levels approaching tap-water quality. Finally, through a resistance breakdown analysis, we identify key design pathways for reducing desalination energy consumption. Together, these results illustrate how decentralized energy storage can be intrinsically coupled to on-site desalination using non-toxic, earth-abundant materials.

2. Experimental

2.1. Chemicals and materials

All chemicals – NaCl, HCl, NaOH, Na_2SO_4, isopropanol – were of analytical grade or higher and were used as received without further purification. Materials used for the preparation of gas diffusion electrodes (GDEs), including 20 wt% Pt/C (Fuel Cell Store, USA) and 5 wt% Nafion solution in ethanol (Ion Power, USA), were also used as received. Gas diffusion electrodes of the cell were using hydrogen (5.0 grade, ≥99.999%, Linde).

An anion-exchange membrane (AEM, Fumasep FAP-450) and a cation-exchange membrane (CEM, PFSA D125—U) (FUMATECH BWT GmbH, Germany) were used throughout this study. Prior to cell assembly, membranes were conditioned in 0.5 M NaCl.

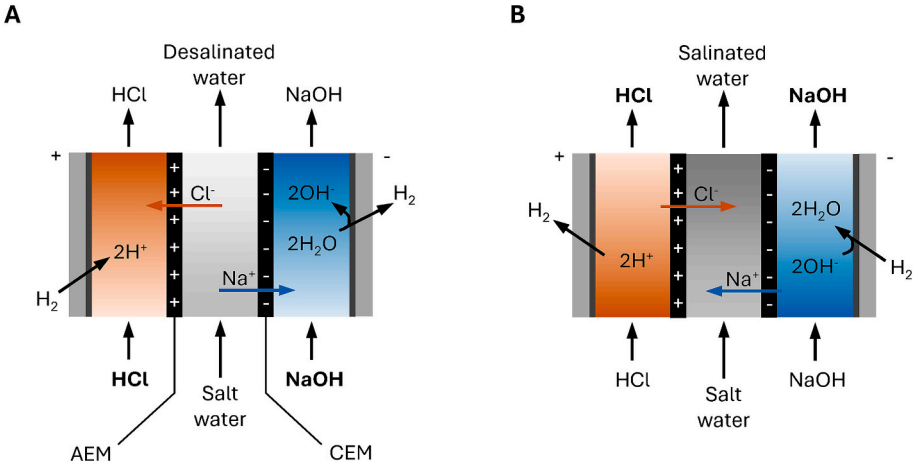

Fig. 1. Scheme of the proposed desalination flow battery during charging (A) and discharging (B) stages.

2.2. Cell design and experimental setup

A custom-built flow cell was used (Fig. S1), consisting of two electrode compartments equipped with GDEs and separated by two ion-exchange membranes, forming a central saline-water compartment. The positive GDE faced the acidic compartment and the AEM, while the negative GDE faced the alkaline compartment and the CEM.

Both electrodes were identical and based on Freudenberg H23CX653 carbon paper loaded with platinum catalyst (0.3 mg(Pt) cm^{-2}) and Nafion ionomer as binder (catalyst-to-ionomer mass ratio of 4:1). Graphite plates with serpentine flow fields served as current collectors and gas distributors and were connected via nickel foil terminals. The electrodes were pressed against PTFE gaskets to ensure sealing.

Electrolyte flow chambers were formed using 3D-printed ABS plates (2 mm thickness) with internal channels, sealed on both sides using 0.5 mm silicone gaskets, resulting in a total chamber thickness of 3 mm. The central saline-water compartment was similarly formed using a 3D-printed ABS frame and separated from the electrode compartments by the AEM and CEM. In each compartment, a stack of polymeric woven spacers (Sefar, Switzerland; thickness 0.48 mm, porosity ~50%; 6 pieces in each chamber) were used to promote uniform flow distribution. The assembled cell was compressed between PMMA end plates and tightened to 3 Nm using a torque wrench.

The experimental setup (Fig. S2) consisted of the flow cell, three electrolyte reservoirs (acid, base, and salt), peristaltic pumps (Masterflex L/S, USA), a hydrogen cylinder, a mass flow controller (Bronkhorst EL-Flow), a gas humidifier (Dreschel bottle filled with deionized water), and an Autolab 302N potentiostat (Metrohm, Switzerland).

To achieve controlled desalination performance, asymmetric electrolyte compositions with balanced charge capacity were employed. A relatively low acid concentration was used in the positive compartment to ensure electrode stability, while a ten-fold higher base concentration was used to balance proton and hydroxide crossover into the central compartment. The initial electrolyte composition corresponding to 0% degree of desalination (DD) consisted of 100 mL of 0.1 M HCl, 20 mL of 0.5 M NaCl, and 10 mL of 1 M NaOH. Degrees of desalination of 0, 25, 50, 75, 90, and 98% were investigated, where DD is defined relative to an initial 0.5 M NaCl solution in the central compartment (see Table 1).

Before electrochemical testing, electrolyte circulation was initiated in all compartments at a flow rate of 6 mL min^{-1}, and the gas sides of the GDEs were purged with nitrogen to remove residual air. Subsequently, humidified hydrogen was supplied at 15 mL min^{-1} (excess of hydrogen was used to ensure low overvoltage for the electrode reactions).

2.3. Electrochemical testing and electrolyte analysis

Prior to each experiment, the open-circuit voltage (OCV, E_{cell} [V]) of the cell was measured and compared with theoretical values calculated as the sum of potential difference between two hydrogen electrodes in acid and base (E_{Nernst} [V]), and Donnan potentials across CEM ($\Delta\phi_{CEM}$ [V]) and AEM ($\Delta\phi_{AEM}$ [V]) [25,27]; note that here we assume no other counter ions for CEM and AEM than Na^+ and Cl^-, respectively:

$$E_{cell} = E_{Nernst} + \Delta\phi_{CEM} + \Delta\phi_{AEM} \quad (4)$$

where

$$E_{Nernst} = \frac{RT}{F}\ln(10)(pH_{base} - pH_{acid}) \quad (5)$$

$$\Delta\phi_{CEM} = \frac{RT}{F}\ln\left(\frac{a_{Na^+,base}}{a_{Na^+,salt}}\right) \quad (6)$$

$$\Delta\phi_{AEM} = \frac{RT}{F}\ln\left(\frac{a_{Cl^-,acid}}{a_{Cl^-,salt}}\right) \quad (7)$$

where pH_{base} and pH_{acid} are pH values in base and acid solutions, respectively, a is activity [M] of an ion with subscript indicates which ion is considered (Na^+ or Cl^-) and in which compartment (*salt*, *base* or *acid*).

Polarization curves were obtained using galvanostatic linear sweeps at a scan rate of 0.1 mA cm^{-2} s^{-1}, sufficiently slow to ensure steady-state conditions. Measurements were performed over voltage windows of OCV − 1.4 V for charging and OCV − 0 V for discharging.

Desalination experiments were conducted galvanostatically, either at open circuit or at a current density of −7 mA cm^{-2} for 3 h, corresponding to approximately 31% desalination of a 0.5 M NaCl solution. Longer experiments until 50, 90, and 98% desalination were not conducted due to hydrogen safety restrictions. During operation, electrolyte samples from the central compartment were periodically collected for ion chromatography (IC) and pH measurements, enabling determination of Na^+ and Cl^- concentrations. The current efficiency of desalination was calculated as the ratio of the measured amount of ions removed to the expected amount, predicted by Faraday's law, assuming ideal ion transport.

Cell resistance (R_{cell}) was determined from the slope of charging polarization curves and decomposed as:

$$R_{cell} = R_{acid} + R_{salt} + R_{base} + R_{CEM} + R_{AEM} \quad (8)$$

Electrolyte resistances (R_{acid}, R_{salt}, *and* R_{base}) were calculated based on compartment geometry, spacer porosity, and concentration-dependent conductivity. Membrane resistances (R_{CEM} and R_{AEM}) were measured independently in a 6-compartment cell (see methodology details elsewhere [28]) for 0.5, 0.25, and 0.01 M NaCl corresponding to 0, 50, and 98% DD, respectively (see Fig. S3).

Specific energy consumption (SEC, kJ mol(NaCl removed)$^{-1}$) during desalination was calculated by combining experimentally determined E_{cell} vs. DD relationships and fitted R_{cell} vs. DD profiles to reconstruct voltage profiles under constant current operation. The energy associated with acid-base neutralization (56 kJ mol^{-1}) was subtracted, as this energy is stored and recovered during discharge. We also analyze average SEC (SEC*) over the course of desalination – from DD 0% to DD 50 or 98% - as a function of current density.

To evaluate the potential of coupled energy storage and desalination, we simulated voltage profiles during charge-discharge cycling. The voltage efficiency (η_V) was defined as the ratio of the average voltage during discharge to that during charge, using the same current density for both steps. The cycle involved charging the cell to achieve 98% desalination degree (DD), followed by replacement of the central compartment electrolyte with fresh feedwater, and subsequent discharge until the acid and base concentrations returned to their initial values.

Finally, an optimistic performance scenario was analyzed by considering improved membranes, thinner electrolyte compartments, and higher porosity flow frames (see details below). Using estimated resistance values for these design improvements, the potential performance gains by calculating SEC and average SEC* for 0–98% desalination. Discharge performance was evaluated using simulated voltage profiles in energy storage mode.

Table 1
Electrolyte composition depending on the DD.

DD, %	C(HCl), M	C(NaOH), M	C(NaCl), M
0	0.1	1	0.5
25	0.125	1.25	0.375
50	0.15	1.5	0.25
75	0.175	1.75	0.125
90	0.19	1.9	0.05
98	0.198	1.98	0.01

2.4. Optimistic resistance case

To highlight the future potential of the device for integrated energy storage and desalination, we also analyzed an optimistic low-resistance scenario. This analysis illustrates how targeted design improvements could significantly reduce overall cell resistance and, consequently, the specific energy consumption of desalination.

We hypothesize that resistance reductions can be achieved through two primary avenues. First, the use of advanced ion-exchange membranes - such as a low-resistance AEM (Fumatech FAS, Cl^- form, 1.03 Ω cm^2 [29]) and a compatible CEM (Fumatech FKS, Na^+ form, 1.5 Ω cm^2 [29]) - would directly lower membrane-related losses. For simplicity, we assume that these resistances remain constant and independent of DD. Second, implementing thinner (0.1 mm) polymer mesh with high porosity (70%) [29], would significantly reduce compartment resistance. This configuration also helps mitigate performance losses due to air entrapment and concentration polarization during operation.

3. Results and discussion

3.1. Concept of the device and battery characteristics

The central concept explored in this work is the use of an acid–base flow battery (ABFB) to intrinsically couple electrochemical energy storage with desalination. In an ABFB, electrical energy is stored through the reversible generation of acid and base, a process that inherently involves salination and desalination of electrolyte streams. As a result, desalinated saltwater is not an external add-on but a natural by-product of battery operation. Here, we extend this concept by proposing that, instead of operating the battery as a fully closed-loop system, partially desalinated or salinated water streams can be selectively extracted or injected, enabling simultaneous energy storage and water purification.

In this study, the battery was operated using NaOH, NaCl (seawater), and HCl electrolytes. At the start of desalination (0% DD), the electrolyte concentrations were 1.0 M NaOH, 0.5 M NaCl, and 0.1 M HCl. While the NaCl concentration reflects typical seawater salinity, a ten-fold higher base concentration relative to acid was intentionally selected to ensure near-zero net acidification of the central compartment and to maintain the chemical stability of the positive electrode. This asymmetric electrolyte configuration enables extended operation without compromising electrode integrity.

During battery charging, electrical energy is converted into chemical energy stored in acid and base, while desalination proceeds simultaneously. Hydrogen oxidation at the negative electrode generates protons in the acidic compartment, whereas hydrogen evolution at the positive electrode produces hydroxide ions in the alkaline compartment. To maintain electroneutrality, Cl^- ions migrate from the central compartment to the acidic side, while Na^+ ions migrate to the alkaline side through the ion-exchange membranes. As charging progresses, the NaCl concentration in the central compartment decreases, while acid and base concentrations increase accordingly. During battery discharging, the electrochemical reactions and ion transport are reversed, resulting in salination of the central compartment.

The electrochemical response of the battery strongly depends on the degree of desalination (Fig. 2A). As NaCl is removed from the central compartment, the open-circuit voltage (E_{cell}) increases from 720 to 896 mV, reflecting the growing pH difference between the alkaline and acidic compartments, which increases from 12.73 to 13.35 (Fig. 2B). Importantly, the experimentally measured open-circuit voltage agrees closely with theoretical predictions across a wide DD range, with deviations below 14 mV for DD values up to 90%. At DD values exceeding 90%, increasing negative deviation of E_{cell} from calculated values are observed, which are attributed to reduced membrane selectivity and enhanced ion crossover at very low salt concentrations. For instance, at 98% DD, calculated Donnan potentials for CEM and AEM account 104 and 47 mV, respectively. This behavior indicates that deep desalination may incur additional energy losses due to non-ideal ion transport.

In parallel, the areal cell resistance evolves with DD (Fig. 2C). From 0% to 75% DD, corresponding to NaCl concentrations decreasing from 0.5 to 0.125 M, the resistance increases moderately from 91 to 130 Ω cm^2. At higher DD values, resistance rises sharply as the central compartment becomes depleted of salt. For example, at 90% DD (0.05 M NaCl), the resistance increases by approximately a factor of three, while further desalination to 0.01 M NaCl (98% DD) leads to a pronounced increase by the factor of 9.3 (to 843 Ω cm^2) compared to the initial value resistance. This sharp rise highlights the dominant role of electrolyte conductivity in governing cell performance at deep desalination levels (see discussion in following sections).

3.2. Current efficiency of desalination and reversible energy storage

Given the coupled concept of energy storage and desalination described above, we now examine the desalination performance of the device in more detail. In particular, we analyze how the composition of the saltwater stream evolves during prolonged operation and to what extent desalination is affected by indirect ion transport processes. To this end, we evaluate voltage profiles together with desalination rates during controlled galvanostatic experiments (Fig. 3).

When no current is applied (Fig. 3A), the open-circuit voltage remains essentially constant over 3 h, indicating negligible electrolyte degradation or spontaneous ion redistribution. This observation is consistent with the minimal changes in salt concentration and pH measured in the central compartment under open-circuit conditions

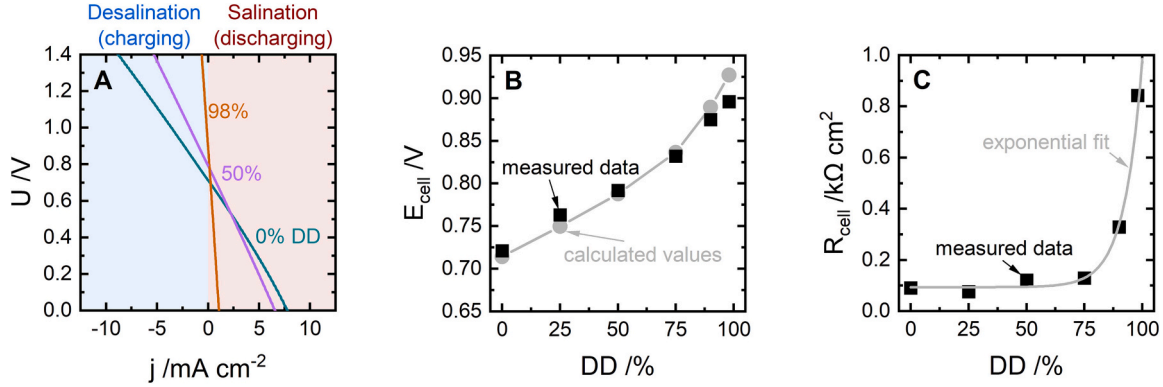

Fig. 2. Polarization curves for charging and discharging of the battery at different DDs (A), and open-circuit voltage, E_{cell} (B), and the cell resistance, R_{cell} (C) depending on the DD; polarization curves were recorded galvanostatically at 0.1 mA cm^{-2} s^{-1} over voltage windows of OCV – 1.4 V for charging and OCV – 0 V for discharging.

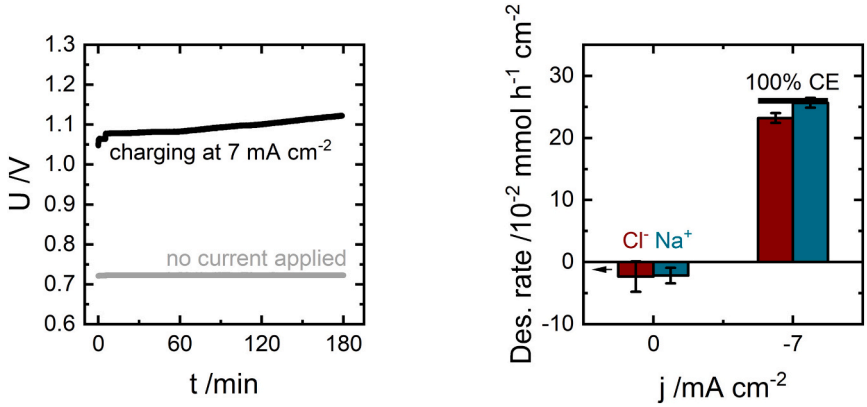

Fig. 3. Cell voltage profiles during 3 h operation at 7 mA cm^{-2} compared with open-circuit conditions (A), and the corresponding desalination derived from electrolyte analysis (B).

(Fig. 3B). Based on the concentration gradients, an increase in Na^+ and a decrease in Cl^- concentrations are expected. While a slight increase in Na^+ is observed, changes in Cl^- are inconclusive. We therefore conclude that at 0 mA cm^{-2}, electrolyte composition in the central chamber remains largely unchanged.

In contrast, when desalination is performed at 7 mA cm^{-2} for 3 h - corresponding to approximately 31% desalination of a 0.5 M NaCl solution - the cell voltage increases steadily with time. This behavior is expected and reflects both the increasing pH difference between the acid and base compartments and the gradual rise in cell resistance as desalination proceeds.

Ion chromatography data (Fig. 3B) reveal high current efficiency for Na^+ and Cl^- transport through the membranes during desalination. The average current efficiency, defined as the ratio of the experimentally removed amount of Na^+ and Cl^- to the amount expected from the applied charge, ranges from 90 to 97% over the 3 h experiment. This indicates that parasitic ion transport and back-diffusion play a minor role under the investigated operating conditions.

An important feature of the proposed device is that, unlike reverse osmosis or electrodialysis, which typically perform most efficiently when treating brackish water [5], the present system is expected to operate most efficiently during partial desalination of seawater. In this regime, the battery operates at relatively low resistance and under moderate concentration gradients across the membranes, which minimizes indirect ion transport and associated efficiency losses.

These results demonstrate that the device is well suited for seawater desalination, particularly at moderate degrees of desalination such as those relevant for pre-desalination or partial salt removal. At higher degrees of desalination, however, the current efficiency is expected to decrease due to steeper concentration gradients and enhanced non-ideal ion transport. The extent of this effect will depend on membrane selectivity, membrane thickness, and electrolyte composition, highlighting the importance of materials selection for deep desalination applications.

It is worth noting that despite using a ten-fold lower acid concentration relative to the base, a slight acidification of the salt compartment is observed for 7 mA cm^{-2} at a rate of $(0.92 \pm 0.24) * 10^{-2}$ mmol h^{-1} cm^{-2}. Since H^+ crossover through the AEM must be accompanied by Cl^- diffusion, the observed net acidification qualitatively aligns with the lower current efficiency for Cl^- removal compared to Na^+. Given the data accuracy at 0 mA cm^{-2} (Fig. 3B), we can confirm H^+ crossover – and possibly OH^- – toward the central compartment, resulting in slight net acidification of the electrolyte. As the above data indicate, the impact of H^+/OH^- crossover on the overall desalination efficiency remains minor.

3.3. Specific energy consumption on desalination

We next analyze the SEC of desalination, which is a key performance metric for desalination technologies. Using interpolated dependences of the cell open-circuit potential (Fig. 2B) resistance (Fig. 2C) as functions of the degree of desalination, we calculate the SEC in units of kJ mol $(NaCl)^{-1}$ as a function of DD (Fig. 4A). This analysis accounts only for electrical energy losses associated with cell voltage and ohmic resistance and does not include energy losses due to ion crossover, losses on electrolyte pumping etc. In addition, the energy required for acid and base formation during desalination (56 kJ mol^{-1}) is excluded from the SEC, as this energy is stored chemically and released during the discharge stage.

Over a wide DD range from 0 to approximately 75%, the SEC increases monotonically with increasing desalination degree (Fig. 4A). In this regime, the rise in SEC is primarily driven by the increasing pH difference between the electrodes and the gradual increase in the cell resistance.

To better understand the origin of this resistance, we performed a breakdown analysis (Fig. 5A) using Eq. (8). This included the measured resistances of the CEM and AEM, along with the calculated contributions from the three electrolyte compartments. We found that at DD values below 50%, the AEM contributes the most to the total resistance, due to the lower conductivity of Fumasep FAP-450 in neutral media (saltwater). At higher DDs, the resistance of the central (saltwater) compartment becomes the dominant contributor to the overall cell resistance.

At deeper desalination levels (Fig. 4A), SEC becomes increasingly dominated by the poor conductivity of the depleted salt solution. For instance, at 90% DD, the central compartment contributes around 38% of the total resistance, rising to 74% at 98% DD. These results highlight the strong dependence of energy consumption on electrolyte conductivity, particularly at high desalination degrees.

We assess average SEC (SEC*) for 0–50% and 0–98% desalination (Fig. 4B), calculated by integrating SEC values from Fig. 4A, to show how it varies with current density. As expected, higher current densities lead to increased SEC due to larger ohmic overpotentials. At 98% DD, the SEC increases from 34 to 92 and 120 kJ $mol(NaCl)^{-1}$ when the current density is increased from 1 to 5 and 7 mA cm^{-2}, respectively. This trend illustrates the trade-off between desalination rate and energy efficiency, particularly at high degrees of desalination.

Because the sharp increase in energy consumption occurs primarily at the later stages of desalination, the choice of the final desalination degree (e.g., 50 vs. 98%) has a limited impact on the average SEC* over a desalination cycle (Fig. 4B). Provided that the cell components remain chemically and mechanically stable, this suggests that the device can, in principle, be operated from seawater salinity down to tap-water levels,

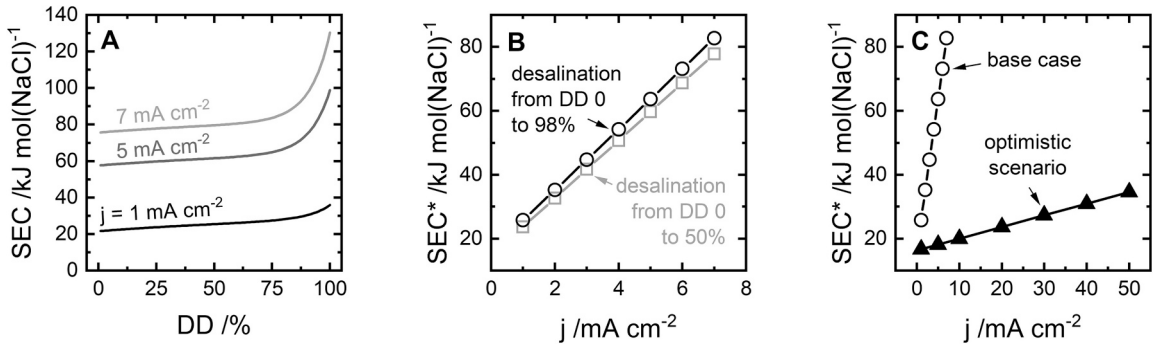

Fig. 4. SEC for desalination as a function of DD (A), average SEC* as a function of current density (B), and comparison between the base case and an optimistic cell resistance scenario for desalination from 0 to 98% DD (C).

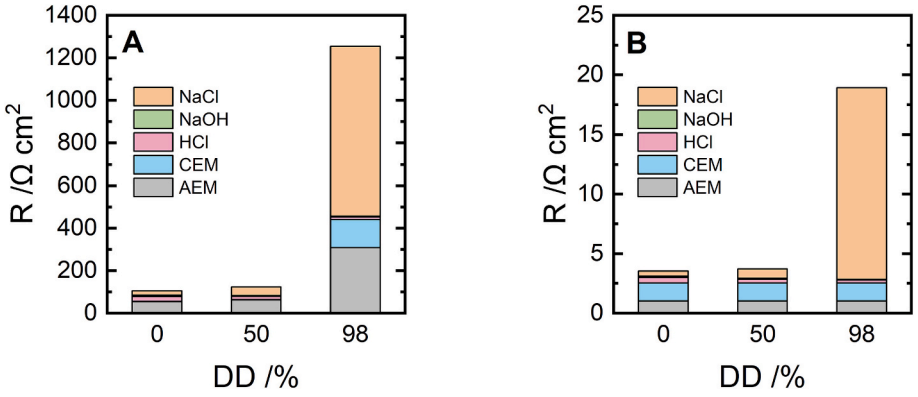

Fig. 5. Resistance breakdown for the base-case cell investigated in this study (A) and a hypothetical optimized cell with reduced component resistances (B); Note: the breakdown shown in (A) is illustrative and does not match the measured resistance values exactly.

consistent with earlier demonstrations in related desalination flow battery systems. However, it should be noted that for DDs discussed here (>50%) the SEC* will be influenced by ion crossover, which is expected to increase as desalination proceeds due to the development of strong Na^+ and Cl^- concentration gradients toward the central compartment.

To assess the potential for further reducing SEC, we compare the experimentally investigated base-case cell with a hypothetical optimistic scenario based on realistic improvements in cell design (Fig. 5B; see Methods for details). In this scenario, thinner flow frames (0.1 mm) and membranes with lower areal resistance are assumed. Under these conditions, the total cell resistance is reduced by approximately a factor of 13 at 0% DD and 20 at 98% DD. Nevertheless, even with such a thin flow frame, the NaCl resistance dominates at 98% DD (Fig. 5B). As a result of the lower resistance, the SEC at 5 mA cm^{-2} decreases from 64 to 18 kJ $mol(NaCl)^{-1}$, while the allowable operating current density range expands almost by order of magnitude to 50 mA cm^{-2} (Fig. 4C). We note that if resistance in the electrolyte compartments is minimized, hydrogen-mediated systems can support reversible neutralization at current densities approaching 100 mA cm^{-2}, as demonstrated in our previous study [27]. These projections highlight the substantial scope for performance improvement through targeted cell optimization and underscore the competitiveness of the proposed concept relative to other desalination flow battery technologies operating at current densities from 0.22 to 15 mA cm^{-2} [12–19].

3.4. Energy storage combined with desalination

To support scalable operation and stable electrochemical performance, we propose a semi-batch desalination mode for the device. In this approach, a portion of seawater is desalinated to a target desalination degree (DD) during the charging stage, after which the partially desalinated stream is extracted and replaced with a fresh batch of feedwater. An illustrative operational cycle is shown in Fig. 6. This configuration also enables dynamic adjustment of current density based on DD, allowing optimization of the trade-off between specific energy consumption and battery power. Alternatively, a continuous mode of operation could be implemented by arranging multiple desalination batteries in series, with feedwater sequentially desalinated in each unit.

During periods of low electricity demand or excess renewable energy availability, the battery stores energy as acid and base while simultaneously desalinating water. This stored energy can later be recovered during discharge, which is accompanied by salination of a new saltwater stream. Under idealized conditions - i.e., symmetric desalination and salination with equal flow rates and current densities - the net water recovery over a full charge-discharge cycle is 50%, comparable to that of conventional seawater desalination systems. We hypothesize that adjusting water recovery, such as using a larger saltwater volume during discharge, could help minimize concentration gradients and thus reduce crossover and electrolyte degradation.

Based on cell performance data, we simulated a complete cycle involving charging to 98% DD, replacement of the central saltwater stream, and discharging back to the original state (0% DD). In the current cell configuration, we observe a modest maximum power density (maximum at the power density vs. current density plot) of 2.2 mW cm^{-2} following saltwater exchange, with a voltage efficiency η_V of 28% at 5 mA cm^{-2}. In contrast, an optimized cell design could reach power densities up to 39 mW cm^{-2} and η_V exceeding 80% at current densities up to 16 mA cm^{-2}. While the power density matches that of the best-performing desalination devices [15,16], it remains at least an order of magnitude lower than conventional redox flow batteries, primarily due to the use of 0.5 M NaCl as electrolyte and three-compartment designs.

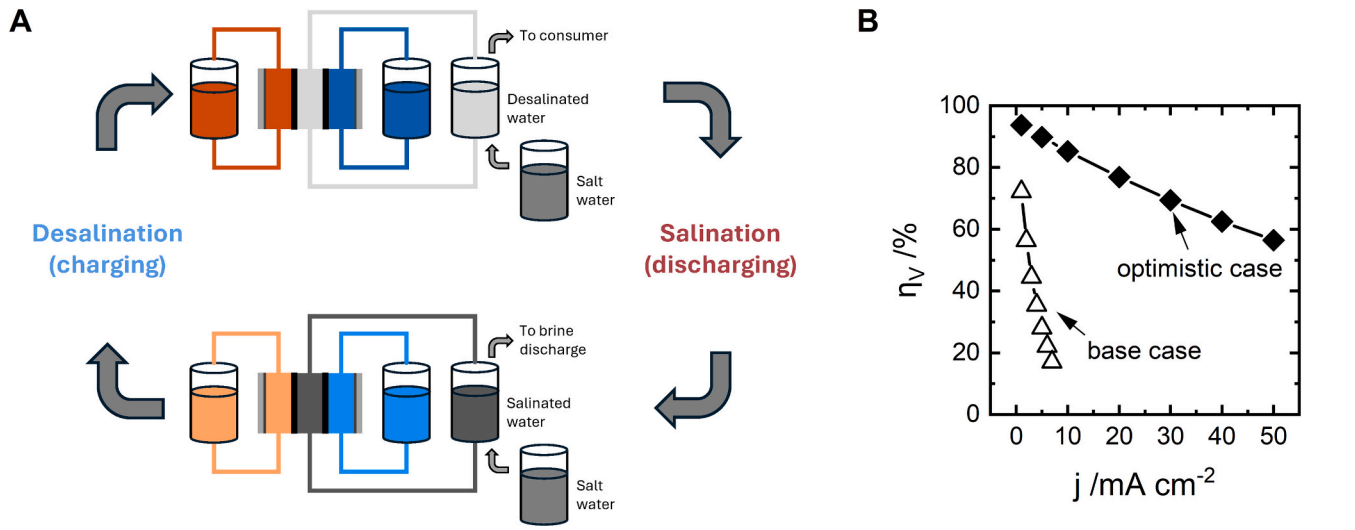

Fig. 6. Illustration of semi-batch battery operation for coupling desalination and energy storage (A) and calculated voltage efficiency (η_V) of the battery as a function of current density (B).

These findings suggest that, provided long-term stability is maintained, the battery can effectively deliver desalination as an added function with minimal energy penalty (see previous section).

3.5. Application areas

To place our device in context, we compared it against state-of-the-art desalination technologies by mapping SEC versus output water purity (Fig. 7; see similar graph with SEC in kWh m^{-3} in SI). This highlights potential implementation niches for the proposed concept. We note that the SEC values presented here reflect lab-scale energy inputs, based solely on cell-level electrical performance. In contrast, system-level SEC - as reported for commercial technologies - typically includes additional

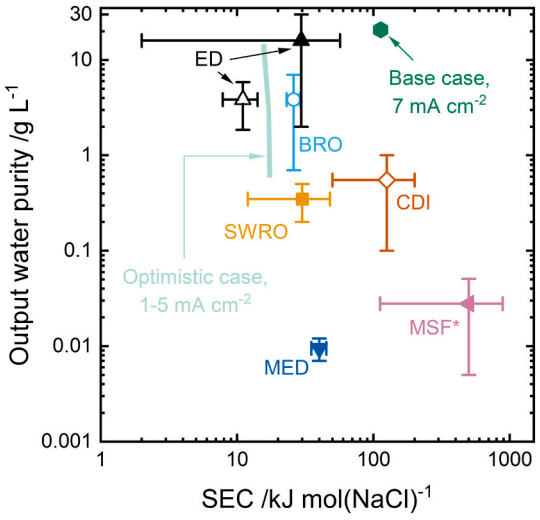

Fig. 7. Performance map of conventional desalination technologies (ED [5,6], BRO [5], SWRO [4], CDI [7,30], MED [8], and MSF [9]) showing SEC versus output water purity. Solid symbols represent systems operating directly on seawater-level salinity (30–35 g L^{-1}), while hollow symbols indicate partial desalination of lower salinity streams (e.g., brackish water), where ED, BRO, and CDI typically perform best. Bars on the graph represent the min/max range for SEC and output water purity. The figure includes both measured SEC for the proposed device and calculated SEC for an optimistic low-resistance scenario (for 1–5 mA cm^{-2}). *Total energy consumption for MSF includes the contribution from thermal energy.

contributions from pumping energy, imperfect ion separation, and other losses. While our SEC estimates do not capture all system losses, they serve to identify trends and feasibility windows for deploying hydrogen-mediated desalination under optimized conditions.

Thermal desalination methods such as MED and MSF can produce high-purity water directly from seawater but incur high energy penalties. CDI offers slightly lower water purity and is typically more effective with pre-desalinated feedwater. While ED is among the most energy-efficient technologies, its performance is optimal with brackish or partially desalinated feedwater, and its energy requirements increase substantially when treating seawater-level salinities.

When plotting the performance of our device, the base case - with relatively high areal resistance - shows SEC around 113 kJ mol(NaCl)$^{-1}$, which is outside the range of leading commercial systems. Due to the low current density in the base case, the device's productivity is expected to be significantly lower than that of conventional desalination systems. However, analysis of an optimized resistance scenario (see Fig. 5B) illustrates significant improvement potential. By adopting best practices in flow cell design - including thinner compartments and low-resistance membranes - our device could achieve SEC values in the range of 15–18 kJ mol(NaCl)$^{-1}$ at moderate current densities (1–5 mA cm^{-2}). At higher currents (e.g., 50 mA cm^{-2}), SEC values of 34 kJ mol(NaCl)$^{-1}$ could still be achieved, substantially improving throughput. These metrics emphasize the promise of hydrogen-mediated desalination, which can operate efficiently without the need for expensive, toxic, or specialty redox-active materials. Moreover, recent studies have shown that hydrogen electrodes can be self-sufficient in hydrogen supply [31,32].

In contrast to other desalination flow batteries [12–19], neutralization flow cells [23–25], and desalination fuel cells [20–22], the use of HCl and NaOH as electrolytes in our system provides logistical advantages. Acid and base electrolyte can be generated and recycled on-site from salt water, enabling desired desalination and energy storage capacity with minimal dependence on external chemical supply chains. Furthermore, unlike many flow cells with capacitive electrodes [33–35], our flow battery architecture allows flexible salt removal capacity and is especially well-suited for treating high-salinity feeds.

That places this hydrogen-mediated desalination battery not as a direct competitor of ED or RO, but rather for a pre-desalination step or for desalination niches without stable energy supply. Our device offers two key advantages over a decoupled system comprising a desalination unit, fuel cell, and electrolyser. First, its dual-purpose architecture eliminates the need for costly hydrogen infrastructure and associated capital expenditures. Second, by avoiding sluggish oxygen reactions, our

system circumvents the round-trip voltage penalty of ~0.4 V expected in electrolyser–fuel cell combinations [26]. This penalty corresponds to an energy loss of approximately 77 kJ mol^{-1} H_2, or ~ 86 kWh m^{-3} of water desalinated (from 30 g L^{-1}) - nearly an order of magnitude greater than the SEC of conventional technologies (<10 kWh m^{-3}; see Fig. S4). While decoupled systems may offer higher productivity, these figures underscore the efficiency advantage of integrating energy storage and desalination while avoiding oxygen electrochemistry.

Hence, given the performance trends and operational flexibility, we propose this system as a possible solution for decentralized desalination and energy storage along coastal regions with intermittent renewable power supply. Specifically, it could serve as a front-end pre-desalination unit, reducing seawater salinity to brackish levels before final purification by downstream technologies such as ED, BRO, or CDI. Additionally, its ability to function under fluctuating power inputs supports its role in addressing the water-energy nexus in off-grid or resource-constrained environments.

3.6. Challenges for practical implementation

To assess feasibility, several technical challenges must be addressed:

A key issue is the crossover of H^+ and OH^- through CEM and AEM, which alters pH in the central compartment. To avoid contamination, it is essential to maintain net-zero acidification - this can be achieved using established strategies from neutralization dialysis [36,37], including tuning concentrations, flow rates, and membrane thickness. Once balanced, crossover only leads to minor energy losses, which can be offset by periodic recharging or electrolyte refreshment.

Electrolyte choice also affects stability. Our selected membranes - Fumasep FAP-450 and PFSA-D125-U - are chemically compatible with their respective environments (AEM is facing acidic compartment, while chemically stable CEM is facing alkaline compartment), and stability is further ensured by avoiding elevated temperatures.

System complexity - three compartments, two membranes, and two reversible hydrogen electrodes - poses a scaling challenge. However, all core components (ion-exchange membranes, GDEs, bipolar plates) are commercially available, and design strategies from fuel cells, electrolysers, and flow batteries are directly applicable. Recent advances in hydrogen-looping systems for acid-base production [31,32,38,39], CO_2 capture [40–42], and energy storage show that efficient, stackable configurations are feasible [39], supported by emerging patents [43–50] and commercial activity (e.g., EDAClabs [51]).

The main cost limitation is the use of platinum group metals. While hydrogen-looping systems are costlier than bipolar membrane-based alternatives, they become viable above ~50–100 mA cm^{-2} [38], where higher productivity offsets capital costs. As shown in this work, better cell design can enable operation in that range. Further cost reductions will require development of platinum metal group-free catalysts [52].

4. Conclusions

In this work, we introduced a new concept for coupling energy storage and desalination using an acid-base flow battery. The core idea relies on the reversible generation of acid and base via H_2 looping during battery charging, which inherently drives the removal of salt from water. Importantly, a significant portion of the energy used for desalination - specifically, the energy of acid-base neutralization (56 kJ $mol(NaCl)^{-1}$) - can be recovered during battery discharge, improving overall energy efficiency. Unlike previously reported desalination flow batteries, our system uses only earth-abundant and non-toxic materials - NaOH and HCl - as electrolytes. It does not rely on external chemical feedstocks, and hydrogen, used as a redox mediator, introduces no harmful crossover while enabling ion transport with minimal voltage penalty on electrode reactions. This design enables scalable desalination and energy storage capacity, as acid and base electrolytes can be regenerated on-site in the required quantities.

Our results show that the resistance of the central (saltwater) compartment is the main limiting factor at higher desalination degrees. Nevertheless, the device achieved 90–97% current efficiency during a 31% reduction in 0.5 M NaCl, with 50% water recovery. These results indicate that the system performs best during partial desalination, where specific energy consumption and ion crossover losses are minimized.

We further showed that applying best practices from the flow cell field - such as thinner membranes and optimized flow compartment design – could improve cycling performance and reduce the specific energy consumption to 14–18 kJ $mol(NaCl)^{-1}$ at moderate current densities (1–5 mA cm^{-2}), with potential for higher productivity at elevated currents (e.g., 50 mA cm^{-2} at doubled specific energy consumption).

We envision this device as a viable component of decentralized energy and water systems, particularly in coastal areas powered by intermittent renewables, addressing the water-energy nexus using environmentally benign and scalable flow battery technology.

CRediT authorship contribution statement

P. A. L. Conceptualization, Methodology, Formal analysis, Preparation of the paper draft, Visualization. A.G.M.D.: Methodology, Formal analysis, Investigation, Visualization, Reviewing and editing of the paper. V.K.: Formal analysis, Reviewing and editing of the paper. D. A. V.: Conceptualization, Formal analysis, Reviewing and editing of the paper, Project administration, Funding acquisition.

Funding sources

NWO-AES Crossover program (RELEASE), project number 17621.

Declaration of competing interest

The authors declare that they have no known competing financial interests or personal relationships that could have appeared to influence the work reported in this paper.

Acknowledgement

This project has received funding from the NWO-AES Crossover program (RELEASE) under project number 17621. The authors thank Christiaan Schinkel, Duco Bosma, Stefan ten Hagen and Kevin Kamman for technical support.

Appendix A. Supplementary data

Supplementary data to this article can be found online at https://doi.org/10.1016/j.desal.2026.120226.

Data availability

Data will be made available on request.

References

[1] WWF Risk Filter Suite v2.0, 2024. https://riskfilter.org/. (Accessed 27 January 2026).
[2] J.J. Urban, Emerging scientific and engineering opportunities within the water-energy nexus, Joule 1 (2017) 665–688, https://doi.org/10.1016/j.joule.2017.10.002.
[3] H. Ritchie, P. Rosado, M. Roser, Energy production and consumption (dataset). https://ourworldindata.org/energy-production-consumption, 2024. (Accessed 27 January 2026).
[4] Y.J. Lim, K. Goh, M. Kurihara, R. Wang, Seawater desalination by reverse osmosis: current development and future challenges in membrane fabrication – a review, J. Membr. Sci. 629 (2021), https://doi.org/10.1016/j.memsci.2021.119292.

[5] S.K. Patel, P.M. Biesheuvel, M. Elimelech, Energy consumption of brackish water desalination: identifying the sweet spots for electrodialysis and reverse osmosis, ACS ES&T Eng. 1 (2021) 851–864, https://doi.org/10.1021/acsestengg.0c00192.
[6] A.H. Galama, M. Saakes, H. Bruning, H.H.M. Rijnaarts, J.W. Post, Seawater predesalination with electrodialysis, Desalination 342 (2014) 61–69, https://doi.org/10.1016/j.desal.2013.07.012.
[7] J.E. Dykstra, S. Porada, A. van der Wal, P.M. Biesheuvel, Energy consumption in capacitive deionization – Constant current versus constant voltage operation, Water Res. 143 (2018) 367–375, https://doi.org/10.1016/j.watres.2018.06.034.
[8] G. Scelfo, A. Trezzi, F. Vassallo, A. Cipollina, V. Landi, C. Xenogianni, A. Tamburini, D. Xevgenos, G. Micale, Demonstration of ultra-high-water recovery and brine concentration in a prototype evaporation unit: Towards zero liquid discharge desalination, Sep. Purif. Technol. 354 (2025), https://doi.org/10.1016/j.seppur.2024.129427.
[9] S.A. Alotaibi, O.M. Ibrahim, F.H. Salamah, Energy and exergy analysis of three major recirculating multi-stage flashing desalination plants in Kuwait, J. Eng. Res. (Kuwait) 13 (2025) 938–948, https://doi.org/10.1016/j.jer.2024.01.019.
[10] D.H. Nam, M.A. Lumley, K.S. Choi, Electrochemical redox cells capable of desalination and energy storage: addressing challenges of the water-energy nexus, ACS Energy Lett. 6 (2021) 1034–1044, https://doi.org/10.1021/acsenergylett.0c02399.
[11] S. Khodadousti, G. Kolliopoulos, Batteries in desalination: a review of emerging electrochemical desalination technologies, Desalination 573 (2024), https://doi.org/10.1016/j.desal.2023.117202.
[12] X. Hou, Q. Liang, X. Hu, Y. Zhou, Q. Ru, F. Chen, S. Hu, Coupling desalination and energy storage with redox flow electrodes, Nanoscale 10 (2018) 12308–12314, https://doi.org/10.1039/c8nr02737d.
[13] G. Mohandass, W. Chen, S. Krishnan, T. Kim, Asymmetric and symmetric redox flow batteries for energy-efficient, high-recovery water desalination, Environ. Sci. Technol. 56 (2022) 4477–4488, https://doi.org/10.1021/acs.est.1c08609.
[14] D. Desai, E.S. Beh, S. Sahu, V. Vedharathinam, Q. Van Overmeere, C.F. De Lannoy, A.P. Jose, A.R. Völkel, J.B. Rivest, Electrochemical desalination of seawater and hypersaline brines with coupled electricity storage, ACS Energy Lett. 3 (2018) 375–379, https://doi.org/10.1021/acsenergylett.7b01220.
[15] C. Debruler, W. Wu, K. Cox, B. Vanness, T.L. Liu, Integrated saltwater desalination and energy storage through a pH neutral aqueous organic redox flow battery, Adv. Funct. Mater. 30 (2020), https://doi.org/10.1002/adfm.202000385.
[16] U. Ghimire, M.K. Heili, V.G. Gude, Electrochemical desalination coupled with energy recovery and storage, Desalination 503 (2021), https://doi.org/10.1016/j.desal.2020.114929.
[17] N. Kim, C.M. Kim, S. Park, J. Park, K.H. Cho, Y. Kim, Continuous desalination and high-density energy storage: Na metal hybrid redox flow desalination battery, Chem. Eng. J. 479 (2024), https://doi.org/10.1016/j.cej.2023.147628.
[18] Q. Liang, F. Chen, S. Wang, Q. Ru, Q. He, X. Hou, C. yuan Su, Y. Shi, An organic flow desalination battery, Energy Storage Mater. 20 (2019) 203–207, https://doi.org/10.1016/j.ensm.2018.11.006.
[19] B. Kim, J.Y. Seo, C.H. Chung, Electrochemical desalination and recovery of lithium from saline water upon operation of a capacitive deionization cell combined with a redox flow battery, ACS ES and T Water 1 (2021) 1047–1054, https://doi.org/10.1021/acsestwater.1c00014.
[20] I. Atlas, S. Abu Khalla, M.E. Suss, Thermodynamic energy efficiency of electrochemical systems performing simultaneous water desalination and electricity generation, J. Electrochem. Soc. 167 (2020) 134517, https://doi.org/10.1149/1945-7111/abb709.
[21] S. Abdalla, S.A. Khalla, M.E. Suss, Scaling up the simultaneous production of clean electricity and clean water, J. Electrochem. Soc. 169 (2022) 063508, https://doi.org/10.1149/1945-7111/ac74e2.
[22] S. Abu Khalla, I. Atlas, S. Litster, M.E. Suss, Desalination fuel cells with high thermodynamic energy efficiency, Environ. Sci. Technol. 56 (2022) 1413–1422, https://doi.org/10.1021/acs.est.1c07288.
[23] Z.M. Bhat, D. Pandit, S. Ardo, R. Thimmappa, A.R. Kottaichamy, N. Christudas Dargily, M.C. Devendrachari, M. Ottakam Thotiyl, An electrochemical neutralization cell for spontaneous water desalination, Joule 4 (2020) 1730–1742, https://doi.org/10.1016/j.joule.2020.07.001.
[24] A. Rani, S.Y. Pan, S. Negi, Y.I. Lin, Electroneutralization desalination with spontaneous chemoelectric power generation, Water Res. 257 (2024), https://doi.org/10.1016/j.watres.2024.121720.
[25] J.J.T. Shibuya, D.E. Macphee, A. Cuesta, Putting stored hydrogen to work without consuming it: A flexible system for energy conversion and water desalination, J. Power Sources 613 (2024), https://doi.org/10.1016/j.jpowsour.2024.234906.
[26] S. Abdalla, S.A. Khalla, M.E. Suss, Voltage loss breakdown in desalination fuel cells, Electrochem. Commun. 132 (2021), https://doi.org/10.1016/j.elecom.2021.107136.
[27] P. Loktionov, D. Konev, A. Antipov, Hydrogen-assisted neutralization flow battery with high power and energy densities, J. Power Sources 564 (2023) 232818, https://doi.org/10.1016/j.jpowsour.2023.232818.
[28] K.V. Petrov, J.W. Hurkmans, R. Hartkamp, D.A. Vermaas, Nanofluidic ion-exchange membranes: Can their conductance compete with polymeric ion-exchange membranes? J. Membr. Sci. 712 (2024) https://doi.org/10.1016/j.memsci.2024.123238.
[29] H.K. Kim, M.S. Lee, S.Y. Lee, Y.W. Choi, N.J. Jeong, C.S. Kim, High power density of reverse electrodialysis with pore-filling ion exchange membranes and a high-open-area spacer, J. Mater. Chem. A Mater. 3 (2015) 16302–16306, https://doi.org/10.1039/c5ta03571f.
[30] M.E. Suss, S. Porada, X. Sun, P.M. Biesheuvel, J. Yoon, V. Presser, Water desalination via capacitive deionization: What is it and what can we expect from it? Energ. Environ. Sci. 8 (2015) 2296–2319, https://doi.org/10.1039/c5ee00519a.
[31] Z.J. Schiffer, É. Lucas, N.B. Watkins, S. Ardo, C. Xiang, H.A. Atwater, Acid and base generation via an electrochemical hydrogen-looping cell tailored for carbon removal applications, Device (2024) 100506, https://doi.org/10.1016/j.device.2024.100506.
[32] D. Xi, Z. Yang, M.S. Emanuel, P. Zhao, M.J. Aziz, Electrochemical acid-base generators for decoupled carbon management, Energ. Environ. Sci. (2025), https://doi.org/10.1039/d4ee05109b.
[33] J. Lee, S. Kim, J. Yoon, Rocking Chair desalination battery based on Prussian Blue electrodes, ACS Omega 2 (2017) 1653–1659, https://doi.org/10.1021/acsomega.6b00526.
[34] S. Arnold, L. Wang, V. Presser, Dual-use of seawater batteries for energy storage and water desalination, Small 18 (2022), https://doi.org/10.1002/smll.202107913.
[35] S. Jeong, Y. Jo, N. Kim, Y. Kim, K. An, Ion-exchange desalination battery with reversible chloride capture, ACS Energy Lett. 9 (2024) 2782–2789, https://doi.org/10.1021/acsenergylett.4c00904.
[36] G.A. Denisov, G.A. Tishchcnko, M. Blcha, L.K. Shataeva, Theoretical analysis of neutralization dialysis in the three-compartment membrane cell, J. Membr. Sci. 98 (1995) 13–25, https://doi.org/10.1016/0376-7388(94)00168-X.
[37] M. Chérif, I. Mkacher, L. Dammak, A. Ben Salah, K. Walha, D. Grande, V. Nikonenko, Water desalination by neutralization dialysis with ion-exchange membranes: Flow rate and acid/alkali concentration effects, Desalination 361 (2015) 13–24, https://doi.org/10.1016/j.desal.2015.01.024.
[38] J.G. Wright, M.W. Kanan, Electrochemical production of >1 M acid and base from neutral salt at high current density and low energy demand, ACS Energy Lett. (2025) 5328–5335, https://doi.org/10.1021/acsenergylett.5c02318.
[39] B.P. Charnay, Y. Chen, J.W. Misleh, J.G. Wright, R.G. Agarwal, E.R. Sauvé, W. L. Toh, Y. Surendranath, M.W. Kanan, Membrane-free electrochemical production of acid and base solutions capable of processing ultramafic rocks, Nat. Commun. (2025), https://doi.org/10.1038/s41467-025-64595-5.
[40] X. Zhang, Z. Fang, P. Zhu, Y. Xia, H. Wang, Electrochemical regeneration of high-purity CO2 from (bi)carbonates in a porous solid electrolyte reactor for efficient carbon capture, Nat. Energy 10 (2025) 55–65, https://doi.org/10.1038/s41560-024-01654-z.
[41] Q. Shu, L. Legrand, P. Kuntke, M. Tedesco, H.V.M. Hamelers, Electrochemical regeneration of spent alkaline absorbent from direct air capture, Environ. Sci. Technol. 54 (2020) 8990–8998, https://doi.org/10.1021/acs.est.0c01977.
[42] S. De Ley, S. Arnouts, K. Van Daele, J. Hereijgers, T. Breugelmans, Feasibility study of an electrochemical hydrogen looping system for indirect ocean capture, Green Chem. 27 (2025) 7137–7146, https://doi.org/10.1039/d4gc05943c.
[43] L. Wen, P. Liu, Y. Sun, Xi Kong, L. Jiang, Power generation method and device based on acid-base neutralization reaction, CN109830731A; CN109830731B, 2019.
[44] A. Cuesta, J. Shibuya, System and process for improving the efficiency of electrolytic hydrogen generation, WO 2024/261191 A1, 2023.
[45] H. Shen, C. Zhou, Y. Liu, C. Wang, Electrochemical hydrometallurgy for sustainable ironmaking, WO 2025/101445 A1, 2023.
[46] C. Wang, H. Shen, C. Zhou, Electrolyzers, US 2024/0035172 A1, 2023.
[47] C.Z.C.S.H. Wang, Electrochemical seawater desalination with hydrogen depolarization, WO2025165609, 2025.
[48] M.W. Kanan, R.G. Agarwal, B.P. Charnay, J.G. Wright, J.W. Misleh, Electrochemical system for generating acidic and basic solutions, WO2025038149, 2024.
[49] Y. Surendranath, R. Zeng, Tang Bryan, R. Bisbey, J. Ufert, Electrochemical hydrogen pumping coupled with catalytic membrane reactor and its applications, WO2025245447, 2025.
[50] H.A. Atwater, Z.J. Schiffer, C. Xiang, S. Ardo, Systems and methods for electrochemical hydrogen looping, US 2024/0133051 A1, 2023.
[51] EDAClabs, (n.d.). https://edaclabs.com/ (accessed April 5, 2026).
[52] S. Bera, H.-J. Woo, H. Khan, S.-Y. Park, J.-H. Baek, W.-J. Lee, S.-H. Kwon, A non-precious hydrogen catalyst coated metallic electrode in an electrochemical neutralization cell for simultaneous fuel and power generation, Chem. Eng. J. 448 (2022) 137716, https://doi.org/10.1016/j.cej.2022.137716.